Review

Check for updates

Authors for correspondence:
David Santos-Carballal
e-mail: SantosCarballalD@cardiff.ac.uk
Nora H. de Leeuw
e-mail: deLeeuwN@cardiff.ac.uk

Reactivity of CO$_2$ on the surfaces of magnetite (Fe$_3$O$_4$), greigite (Fe$_3$S$_4$) and mackinawite (FeS)

David Santos-Carballal[1], Alberto Roldan[1], Nelson Y. Dzade[2] and Nora H. de Leeuw[1,2]

[1]School of Chemistry, Cardiff University, Main Building, Park Place, Cardiff CF10 3AT, UK
[2]Department of Earth Sciences, Utrecht University, Budapestlaan 4, 3584 CD Utrecht, The Netherlands

DS-C, 0000-0002-3199-9588; AR, 0000-0003-0353-9004;
NYD, 0000-0001-7733-9473; NHdL, 0000-0002-8271-0545

The growing environmental, industrial and commercial interests in understanding the processes of carbon dioxide (CO$_2$) capture and conversion have led us to simulate, by means of density functional theory calculations, the application of different iron oxide and sulfide minerals to capture, activate and catalytically dissociate this molecule. We have chosen the {001} and {111} surfaces of the spinel-structured magnetite (Fe$_3$O$_4$) and its isostructural sulfide counterpart greigite (Fe$_3$S$_4$), which are both materials with the Fe cations in the 2+/3+ mixed valence state, as well as mackinawite (tetragonal FeS), in which all iron ions are in the ferrous oxidation state. This selection of iron-bearing compounds provides us with understanding of the effect of the composition, stoichiometry, structure and oxidation state on the catalytic activation of CO$_2$. The largest adsorption energies are released for the interaction with the Fe$_3$O$_4$ surfaces, which also corresponds to the biggest conformational changes of the CO$_2$ molecule. Our results suggest that the Fe$_3$S$_4$ surfaces are unable to activate the CO$_2$ molecule, while a major charge transfer takes place on FeS{111}, effectively activating the CO$_2$ molecule. The thermodynamic and kinetic profiles for the catalytic dissociation of CO$_2$ into CO and O show that this

THE ROYAL SOCIETY
PUBLISHING

2

process is feasible only on the FeS{111} surface. The findings reported here show that these minerals show promise for future CO_2 capture and conversion technologies, ensuring a sustainable future for society.

This article is part of a discussion meeting issue 'Providing sustainable catalytic solutions for a rapidly changing world'.

1. Introduction

Mitigating the increasing concentration of CO_2 to sustainable levels and preventing excessive anthropogenic emissions of this molecule to reach the atmosphere are currently two major scientific and political challenges in most of the countries which signed the Paris Agreement [1,2]. CO_2 has been linked directly to global warming due to its powerful heat-trapping properties [3,4]. However, CO_2 is also a potential chemical feedstock that can be harnessed from industrial sources for a myriad of uses, thereby improving the global carbon cycle [5–9]. One of the most important examples of CO_2 utilization is as raw material for the manufacturing of a wide variety of added-value products such as carbamic acids [10–13], carbonates [14], polycarbonates [15–22] and liquid fuels [23–28].

The chemical conversion of CO_2 can be classified according to the energy associated with the reaction as (i) low-energy processes and (ii) high-energy processes [29]. The low-energy processes are clearly the most energetically favourable cases, where the entire CO_2 moiety is integrated into an electron-rich compound, in which the formal 4+ oxidation state of the C atom may change to 3+. However, reducing the C oxidation state by more than one unit to transform the very stable CO_2 molecule into chemicals is always strongly endothermic, as this molecule is the end product of the aerobic chemical and biological combustion processes. For the high-energy processes, the key to the success of CO_2 conversion at industrial scale is the use of stable, non-toxic, reusable and efficient catalysts that provide the electrons via active sites to activate and convert the molecule chemically [5,7,8].

The spinel-structured magnetite (Fe_3O_4) is an iron oxide used as the main component of industrial heterogeneous catalysts because of its stability, availability and low cost. The Fe ions of Fe_3O_4 have a mixed valence state (2+/3+), which allows this material to catalyse both oxidation/reduction and acid/base reactions [30]. For instance, Fe_3O_4 is part of the catalysts used in the Haber–Bosch process for the production of ammonia NH_3 [31]. During this process, Fe_3O_4 is reduced *in situ* by H_2 into the catalytically active α-Fe [32], where the adsorption and dissociation of the highly stable N_2 molecule takes place [33,34]. Similarly as in the CO_2 conversion process, the adsorption and activation of N_2 is the rate-limiting step in the mechanism of NH_3 formation [35–39]. Fe_3O_4 is also used in the Fischer–Tropsch process for the conversion of syngas (a mixture of CO and H_2) into hydrocarbons [40]. However, experiments suggest that the working catalyst is only achievable once Fe_3O_4 is exposed to the syngas and is partially reduced to a mixture of α-Fe and iron carbide (χ-Fe_5C_2) with a high quantity of remnant Fe_3O_4 [41]. Another mineral with Fe in the most oxidized form is Fe_2O_3, which is the initial catalyst of the water gas shift (WGS) reaction supplying H_2 to the Haber–Bosch and Fischer–Tropsch processes [40]. However, the catalyst becomes active only after it is carefully reduced to Fe_3O_4 by the initial syngas mixture, avoiding over-reduction to α-Fe and χ-Fe_5C_2 [42].

Greigite (Fe_3S_4) is the isostructural sulfide counterpart of Fe_3O_4 with the Fe ions also in the mixed valence state, while mackinawite (tetragonal FeS) has these cations in the lowest possible coordination and 2+ oxidation state. The structural analogy between Fe_3S_4 and FeS with certain contemporary enzyme co-factors in the form of Fe_4S_4 cubane clusters [43] has led to the suggestion that these minerals could have played an important catalytic role in the primordial metabolism by converting the CO_2 molecule into small chemicals [44–46]. According to the iron–sulfur origin of life theory [47,48], the first organic molecules were then formed after the reduction of CO_2 catalysed by the oxidation of Fe^{2+} ions probably through a mechanism similar to the modern-day acetyl coenzyme A pathway [43–46,49]. A recent study combining experiments and

computational simulations has shown the electro-reduction of CO_2 on Fe_3S_4 into small organic molecules [50], supporting the iron–sulfur origin of life theory. Simulations of FeS have also predicted that the surfaces of this mineral activate and dissociate the CO_2 molecule [51].

The purpose of this report is to present density functional theory (DFT) simulations that we have carried out to elucidate the trends of CO_2 adsorption, activation and dissociation on the surfaces of Fe_3O_4, Fe_3S_4 [50,52] and FeS [51] and compare them with recent experiments. We have taken into account the impact of the anions, stoichiometric and structural differences of the materials and related them to explain the performance towards CO_2 conversion. We have rationalized the dependence of the adsorption energies and the charge donated by the surface to the molecule in the adsorbed geometries. We have also discussed the differences between the simulated wavenumbers for the fundamental vibrational modes of the isolated and adsorbed CO_2 to explain the weakening of the C–O bond and the activation of this molecule. We propose the kinetic and thermodynamic mechanisms that account for the unimolecular dissociation of the chemisorbed and activated states of the CO_2 molecule. These mechanisms are described in terms of the activation energy required to reach the transition state and the overall energy associated with the fragmentation of the CO_2 molecule into CO and O. The catalytic properties of the Fe_3O_4, Fe_3S_4 and FeS towards carbon activation could lead to economically viable applications to convert industrially produced CO_2 into fine chemicals and fuels.

2. Density functional theory calculations

(a) Calculation details

We have carried out spin-polarized calculations with the Vienna *ab initio* simulation package (VASP) [53–56]. At the level of the generalized gradient approximation, the exchange–correlation in the form of the Perdew–Burke–Ernzerhof (PBE) [57,58] functional was used to model Fe_3O_4, while the Perdew–Wang 91 (PW91) [59,60] functional was used together with the spin interpolation formula of Vosko *et al.* [61] for the simulation of the sulfide phases, to remain consistent with previous reports. The long-range van der Waals (vdW) interactions were included via the semiempirical method of Grimme (D2) [62], using the global scaling factor parameter optimized for the PBE functional, $s_6 = 0.75$, which is known to describe appropriately the adsorption properties in oxides [63,64] and sulfides [51,65–69]. The projector augmented wave (PAW) method was used to describe the core electrons and their interaction with the valence ones [70,71]. The frozen cores of the Fe, O, S and C atoms were defined up to and including the 3p, 1s, 2p and 1s electrons, respectively. Kohn–Sham valence states were expanded in a plane-wave basis set with a cutoff for the kinetic energy of 400 eV for Fe_3O_4 [63] and FeS [51,66,69,72,73], and fixed at 600 eV for Fe_3S_4 [50,52,74–79], in agreement with previous publications. The Brillouin zone integrations of the surface slabs were performed using a Γ-centred Monkhorst–Pack grid of $5 \times 5 \times 1$ k-points for the simulation of all the materials considered. A Hubbard Hamiltonian [80] in the version of Dudarev *et al.* [81] was used for the description of the localized and strongly correlated d Fe electrons of the spinel materials, while we found that it is not needed to describe the properties of FeS correctly [51,66,69,72,73,82]. Following previous works, we have chosen $U_{eff} = 3.7$ eV for Fe_3O_4 [63] and 1.0 eV for Fe_3S_4 [50,75,76,83]. Dipole corrections were applied perpendicularly to the surfaces to improve the electronic convergence due to the dipole moments formed by the CO_2 when added to the surface [84,85]. The atomic positions were relaxed to their ground state using the conjugate-gradient method until the Hellmann–Feynman forces on all atoms dropped below 0.02 eV Å^{-1}. The electronic partial occupancies were determined using the tetrahedron method with Blöchl corrections to increase the integration efficiency for all the calculations [86]. A Bader charge analysis was used to integrate the electronic density into atomic charges, as implemented by Henkelman and co-workers [87–89]. The charge density difference schemes were constructed by subtracting the sum of the electron charge densities of the clean surface and isolated adsorbate, with identical structure as in the adsorbed form, from the electron density of the total adsorbate–surface system obtained from single-point calculations.
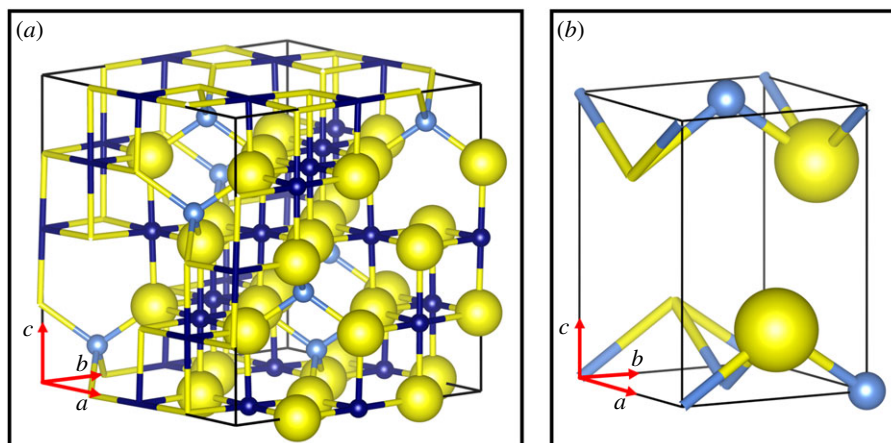
Figure 1. (*a*) Conventional unit cell of Fe_3S_4 showing the cubic spinel crystal structure. Note that Fe_3O_4, the isostructural oxide counterpart of Fe_3S_4, is not displayed. (*b*) Schematic of the tetragonal unit cell of FeS. Tetrahedral Fe_A atoms are in light blue, octahedral Fe_B atoms are in dark blue and S atoms are in yellow. Atoms belonging to the neighbouring unit cells are represented as sticks. (Online version in colour.)

The climbing image nudged elastic band method (ci-NEB) [90–94] was used to search the transition states and the reaction barriers for the dissociation of the CO_2 molecule, which were characterized by a single imaginary frequency along the reaction coordinate. For the ci-NEB calculations, six structures were linearly interpolated between the geometrically optimized initial (reactants) and final states (products), which were minimized as a string of images. The exact transition state corresponds to the image with the highest energy that is driven up to the saddle point, maximizing its energy along the minimum energy path.

The spinel phases, i.e. Fe_3O_4 and Fe_3S_4, belong to the space group $Fd\bar{3}m$ (no. 227), which comprises 56 atoms (figure 1*a*) [95,96]. The face-centred cubic unit cell contains 32 anions in a cubic close-packed arrangement with eight of the tetrahedral holes (*A*) and 16 of the octahedral (*B*) ones filled by the Fe atoms. Both spinels have an inverse electronic distribution of the Fe ions that can be expressed as $Fe_A{}^{3+}[Fe^{2+}Fe^{3+}]_B X_4{}^{2-}$, where X represents the O or S anion, meaning that 50% of the Fe^{3+} cations are occupying the *A* holes and the rest along with all the Fe^{2+} atoms are filling the *B* sites [97–101]. For the spinel-structured materials, all the calculations were spin-polarized and the initial magnetic moments were set following a high-spin ferrimagnetic structure, with the spin moments of the atoms filling the *A* and *B* holes oriented antiparallel, in agreement with previous studies [75,76,102,103].

FeS has a tetragonal crystal structure characterized by the space group $P4/nmm$ (no. 129) [104–106]. The tetragonal unit cell is composed of two Fe and two S atoms. The cations are located at the centre of the square sides and at the corners of the unit cell, while the anions are occupying the rectangular faces on opposite sides of the unit cell (figure 1*b*). Bulk FeS is a layered material with sheets lying in the *ab*-plane of perfectly square-planar coordinated Fe atoms which are tetrahedrally coordinated by four equidistant S atoms. The anions appear above and below the cation sheets, holding the layers together by vdW forces. We did not consider the spin-polarization effect for the simulation of FeS as we have found it not to have any meaningful effect in the electronic structure of this material [51,66,69,72,73,82].

(b) Surface models

The slab models were built following the dipole method, which is based on the condition that the net dipole perpendicular to the surface must be zero, as determined by Tasker [107]. All the surfaces studied were generated by cutting the optimized bulk of the iron minerals using the METADISE code [108]. We considered the {001} and the {111} surfaces for each of the

Table 1. Surface area (A_{surf}) in Å^2, total number of atomic layers (N_{lay}) and total number of atoms (N_{atom}) for the slabs of Fe_3O_4, Fe_3S_4 and FeS.

mineral	surface	A_{surf}	N_{lay}	N_{atom}
Fe_3O_4	{001}	70.5	9	56
	{111}	61.1	13	56
Fe_3S_4	{001}	93.5	9	56
	{111}	81.0	13	56
FeS	{001}	51.4	6	32
	{111}	111.9	9	48

iron-based materials. A separation of $12\,\text{Å}$ and $15\,\text{Å}$ was added to the direction perpendicular to the surface plane between the simulation slab of the spinel materials and FeS, respectively, and its periodically repeated image, ensuring they did not interact. Convergence tests with respect to the surface slab and vacuum thickness, as well as the number of relaxed atomic layers, were performed until the energy was constant within $1\,\text{meV}$ of accuracy. Table 1 shows the surface area, the total number of atomic layers and the total number of atoms of the most stable surface slab models used in the simulations of the three iron-based materials. The {001} surface of the isostructural spinel minerals terminates in a layer comprising both anions and five-fold coordinated Fe_B atoms. However, while the Fe_3O_4{001} surface has three-fold coordinated Fe_A ions with the $(\sqrt{2} \times \sqrt{2})R45°$ symmetry above the top-most sulfur layer, these ions move into the subsurface layer in Fe_3S_4, retaining the tetrahedral coordination. The {111} surfaces are identically finished in a bulk-like layer of anions forming a hexagonal honeycomb pattern in Fe_3O_4 with two Fe_A per every Fe_B ion sitting above it [63,109], whereas in Fe_3S_4 these cations relax into the subsurface layer. The FeS{001} and {111} surfaces terminate in a S layer with four-fold and three-fold coordinated Fe_A atoms, respectively, in the subsurface layer. The lower half of the slabs was kept fixed at the optimized bulk geometry, while the exposed upper half was allowed to relax without restrictions for each simulation slab. Note that we did not consider the effect of defects or environmental species during our simulations, which are known to increase the reactivity of the surfaces, as this is outside the scope of this work, which is concerned with the comparison between two isostructural materials, Fe_3O_4 and Fe_3S_4, to compare the relative effects of oxygen and sulfur, and between two different sulfides, Fe_3S_4 and FeS, which contain iron in different valence states.

(c) Simulation of the vibrational modes

The vibrational frequencies were calculated for the isolated and adsorbed CO_2 molecule and for its dissociation fragments, i.e. CO and the O atom, by means of the central finite differences approach. This method comprises the calculation of the vibrational frequencies from the second derivative of the potential energy with respect to the atomic positions, which are moved by a small negative and positive displacement for each Cartesian coordinate, ensuring they are contained within the harmonic part of the potential well. We have defined the vibrationally active atoms as those belonging to the adsorbate for the iron sulfide materials and also included the top-most layers of the surface slab for Fe_3O_4. The coupling between the surface phonons and the vibrational frequencies of adsorbates, all of which appear above $500\,\text{cm}^{-1}$, was neglected.

(d) Thermodynamic and kinetic profiles

We have calculated the adsorption energy (E_{ads}) of the CO_2 molecule on the {001} and {111} surfaces of Fe_3O_4, Fe_3S_4 and FeS as

$$E_{ads} = E_{CO_2+surf} - (E_{CO_2} + E_{surf}), \tag{2.1}$$

where E_{CO_2+surf} is the total energy of the CO_2 molecule interacting with the surfaces, E_{CO_2} is the energy of the isolated CO_2 molecule and E_{surf} is the energy of the naked surface slab.

We have proposed the CO_2 dissociation mechanism as a single elementary step taking place on the {001} and {111} surfaces of Fe_3O_4, Fe_3S_4 and FeS. The activation energy (E_{act}) was obtained from the difference between the energy of the transition state (E_{TS}) and the initial state, i.e. the molecularly adsorbed CO_2 on the mineral surface (E_{CO_2+surf}), as

$$E_{act} = E_{TS} - E_{CO_2+surf}. \tag{2.2}$$

The dissociation energy (E_{diss}) was defined as the energy difference between the final CO_2 dissociated state, i.e. the CO + O product fragments ($E_{CO+O+surf}$), and the molecularly adsorbed CO_2 as

$$E_{diss} = E_{CO+O+surf} - E_{CO_2+surf}. \tag{2.3}$$

Note that all the energies for Fe_3O_4 were corrected by the vibrational zero-point energy (E_{ZP}). E_{ZP} was approximated to $\sum_i h\nu_i/2$, where h is Planck's constant and ν_i are the fundamental vibrational frequencies of the normal modes.

3. Results and discussion

(a) Adsorption structures of CO_2

As a first step, the adsorption of the CO_2 molecule was studied on the {001} and {111} surfaces of each material. We have carried out a comprehensive investigation of the initial guess adsorption sites on the surfaces, as well as the possible geometries and orientations of the pre-activated (bent) CO_2 molecule, before performing the full optimization of the adsorption structures and energies. The potential adsorption sites included the atop, bridge and hollow positions between the non-equivalent surface atoms, with the CO_2 molecule being placed both flat and perpendicular to the surface and coordinating as many surface atoms as possible. In what follows, we only discuss and compare the results of the most favourable CO_2 adsorption modes for each surface, i.e. those releasing the largest adsorption energy. The most important parameters characterizing the adsorption modes are shown in table 2. Our simulations indicate that the C atom coordinates one of the O surface atoms (O_{surf}) of Fe_3O_4, but prefers to bind one of the Fe_A ions of FeS. In the case of Fe_3S_4, the carbon atom binds surface S or Fe_B atoms depending on the surface, as displayed in table 2. The interactions are also given by the elongation of the intramolecular CO bond and the proximity between the molecular O atoms and the surface Fe ions.

(i) Magnetite

We found that CO_2 interacts strongly with both the Fe_3O_4{001} and {111} surfaces, where the molecule bends and forms a highly stable carbonate-shaped group upon interaction with the surface (table 2 and figure 2). Our calculations indicate that the C atom sits atop the surface oxygen, while the oxygens from the molecule point towards the undercoordinated Fe_A and Fe_B ions, in agreement with recent computational and experimental studies on CO_2 adsorption on the Fe_3O_4{001} and {111} surfaces [110–112]. This interaction induces a practically equal elongation of both intramolecular C−O distances by 0.09 Å with respect to the isolated molecule. The strongest adsorption of the CO_2 molecule with any of the three minerals discussed here takes place on the Fe_3O_4{111} surface, as summarized in table 3. For the interaction with the {111} surface, both O atoms from the CO_2 coordinate to the Fe_B cations as shown in figure 2. Moreover, the C atom coordinates to one surface oxygen atom at 1.40 Å, which induces a tilt of the CO_2 molecule with respect to the surface normal, as the three coordinating atoms in the surface are not in a straight line.
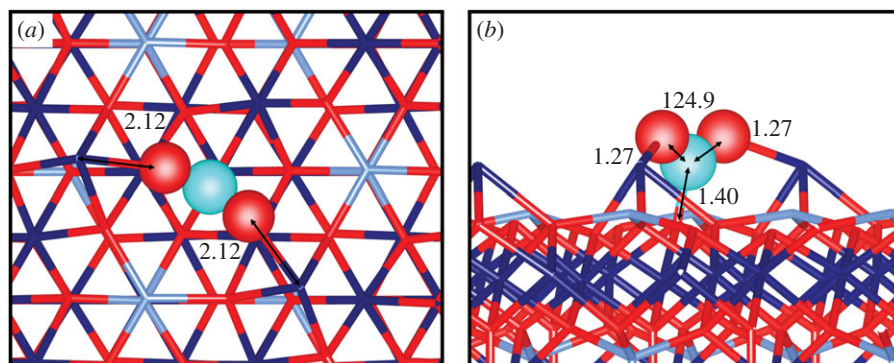
Figure 2. CO_2 adsorbed to the $Fe_3O_4\{111\}$ surface, showing (a) top view and (b) side view. Tetrahedral Fe_A atoms are in light blue, octahedral Fe_B atoms are in dark blue, C atoms are in cyan and O atoms are in red. Surface atoms are represented as sticks and the CO_2 molecule is represented as balls and sticks. Interatomic distances are shown in Å and angles are shown in °. (Online version in colour.)

Table 2. Interatomic distances (d) in Å and bond angles ($\angle$) in ° for the energetically preferred CO_2 adsorption configurations on the $\{001\}$ and $\{111\}$ surfaces of Fe_3O_4, Fe_3S_4 [50,52] and FeS [51]. O_1 and O_2 represent O atoms of the CO_2 molecule, while X_{surf} represents one of the surface anions.

mineral	surface	$d(C-O_1)$	$d(C-O_2)$	$d(C-[Fe, X_{surf}])$	$d(O_1-[Fe, X_{surf}])$	$d(O_2-Fe)$	$\angle(OCO)$
CO_2 (isolated molecule)		1.18	1.18	—	—	—	180.0
Fe_3O_4	$\{001\}$	1.27	1.27	1.39 [O_{surf}]	2.03 [Fe_A]	2.15 [Fe_B]	128.9
	$\{111\}$	1.27	1.27	1.40 [O_{surf}]	2.12 [Fe_B]	2.12 [Fe_B]	124.9
Fe_3S_4	$\{001\}$	1.18	1.17	3.31 [S_{surf}]	2.96 [S_{surf}]	—	179.2
	$\{111\}$	1.18	1.17	3.14 [Fe_B]	2.27 [Fe_B]	—	179.4
FeS	$\{001\}$	1.18	1.18	4.01 [Fe_A]	4.22	4.15	179.6
	$\{111\}$	1.24	1.24	2.11 [Fe_A]	2.11	2.11	138.7

Table 3. CO_2 adsorption energies (E_{ads}) in eV and surface energies (γ) in J m^{-2} of the $\{001\}$ and $\{111\}$ surfaces of Fe_3O_4 [63], Fe_3S_4 [50,52,78] and FeS [51,66,69].

mineral	surface	E_{ads}	γ
Fe_3O_4	$\{001\}$	−1.03	0.96
	$\{111\}$	−1.37	1.10
Fe_3S_4	$\{001\}$	+0.18	0.60
	$\{111\}$	−0.19	0.90
FeS	$\{001\}$	−0.20	0.19
	$\{111\}$	−0.87	1.51

(ii) Greigite

Our calculated results showed that the CO_2 molecule preferably adsorbs on the $Fe_3S_4\{111\}$ surface (table 2). Unlike the trends discussed for Fe_3O_4, we found that the CO_2 molecule remained linear upon adsorption to either the $Fe_3S_4\{001\}$ or $\{111\}$ surface, indicating a weak interaction, as shown
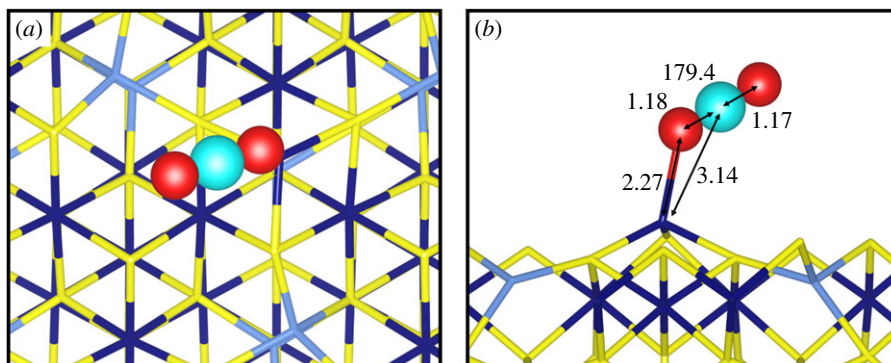
Figure 3. CO_2 adsorbed to the Fe_3S_4{111} surface, showing (a) top view and (b) side view. Tetrahedral Fe_A atoms are in light blue, octahedral Fe_B atoms are in dark blue, S atoms are in yellow, C atoms are in cyan and O atoms are in red. Surface atoms are represented as sticks and the CO_2 molecule is represented as balls and sticks. Interatomic distances are shown in Å and angles are shown in °. (Online version in colour.)
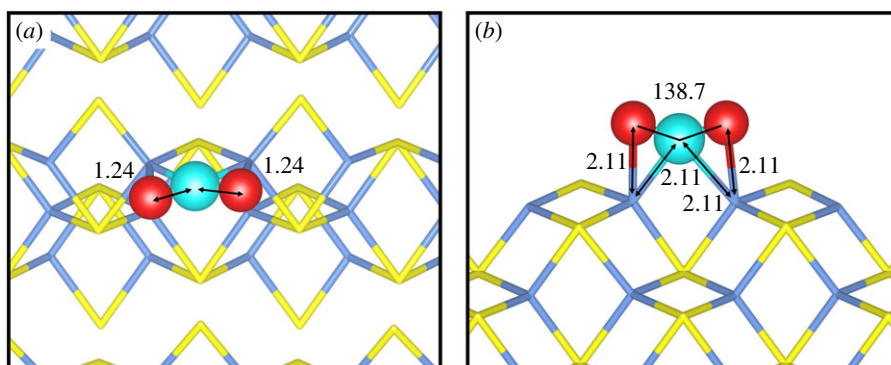
Figure 4. CO_2 adsorbed to the FeS{111} surface, showing (a) top view and (b) side view. Tetrahedral Fe_A atoms are in light blue, S atoms are in yellow, C atoms are in cyan and O atoms are in red. Surface atoms are represented as sticks and the CO_2 molecule is represented as balls and sticks. Interatomic distances are shown in Å and angles are shown in °. (Online version in colour.)

in figure 3. Our simulations suggest that the large electrostatic repulsions between the electronic clouds of the surface sulfur atoms and the electronic lone pairs located on the O atoms from the CO_2 prevent this molecule from binding to the {001} surface. On the other hand, one of the O atoms coordinates to an undercoordinated Fe_B cation from the Fe_3S_4{111} surface, anchoring the CO_2 molecule, which remains without geometrical or electronic changes [50,52].

(iii) Mackinawite

The strongest interaction between the CO_2 molecule and FeS is with the {111} surface (tables 2 and 3). In terms of the adsorption modes, the three atoms of the CO_2 molecule bind to the FeS{111} surface, as shown in figure 4. The CO_2 molecule displays a bent conformation and the intramolecular C—O distances are equally stretched by 0.06 Å compared to the isolated molecule. The CO_2 molecule was physisorbed on the FeS{001} surface, although no evidence was found for any structural change of either the adsorbate or the {001} mineral surface, as the CO_2 was only weakly adsorbed. The large difference between adsorption energies inferred for the FeS{001} and {111} surfaces suggests that its value strongly depends on the possibility of the CO_2 molecule bending and coordinating several surface atoms [51].

Table 4. Charge difference ($\triangle q$) in e^- for CO_2 between the neutral state of the isolated molecule and after adsorption to the {001} and {111} surfaces of Fe_3O_4, Fe_3S_4 [50,52,78] and FeS [51,66,69] and the simulated wavenumbers in cm^{-1} of the fundamental vibrational modes of the isolated and adsorbed CO_2 molecule on the iron mineral surfaces. The experimental vibrational modes of the gas-phase CO_2 molecule are also shown [113]. The work function (Φ) values in eV of the naked surfaces are also provided. Negative values of $\triangle q$ indicate charge transfer from the surface to the adsorbate. The presented vibrational modes are the asymmetric stretching (ν_{asym}), symmetric stretching (ν_{sym}) and bending (δ) modes.

| mineral	surface	$\triangle q$	Φ	ν_{asym}	ν_{sym}	δ
CO_2 (isolated molecule)				2373	1323	631
CO_2 (gas phase)				2349	1333	667
Fe_3O_4	{001}	−0.17	4.22	1601	1259	703
	{111}	−0.27	3.90	1547	1248	669
Fe_3S_4	{001}	0.0	5.13	2355	1313	615
	{111}	0.0	5.04	2363	1311	608
FeS	{001}	0.0	4.72	2349	1319	628
	{111}	−0.80	3.68	1764	1173	654

(b) Adsorption energies of CO_2

Table 3 summarizes the calculated adsorption energies of the CO_2 molecule along with electronic parameters of the {001} and {111} surfaces of Fe_3O_4, Fe_3S_4 and FeS, showing any correlations. It is evident that the surfaces of sulfides are the least favourable for the adsorption of the CO_2 molecule [50]. The value of our adsorption energy (1.37 eV) calculated for the most favourable interaction of the CO_2 molecule with the Fe_3O_4{111} surface, is in excellent agreement with a recent computational study [110]. On both iron sulfides, the CO_2 molecule is most likely to interact linearly, with the exception of the FeS{111} surface, leading to smaller adsorption energies than on the Fe_3O_4 surfaces. This different behaviour can be rationalized in terms of the anion strength, which allows coordination with the C atom, forming a species that resembles a carbonate group on the oxide. The electronic delocalization of the π molecular orbital, belonging to the pseudo-carbonate group formed on the Fe_3O_4{001} and {111} surfaces, also plays a significant role in the stabilization of this adsorption mode. The non-hybridized atomic p_z orbitals lying perpendicular to the carbonate plane can overlap effectively only with surface oxygens, as the sulfur atoms have more extended orbitals. The adsorption energy is also related to the surface energy (γ), as the CO_2 molecule releases the largest adsorption energy upon interaction with the least stable surface of each material. Our simulations also suggest that the adsorption energies strongly depend on the variation of the bond angle upon CO_2 interaction with the surfaces (tables 2 and 3).

(c) Charge transfer characterization

We have estimated the charge transfer ($\triangle q$) between the mineral surfaces and the CO_2 molecule from the variation of the atomic Bader charges. The adsorbate gains electronic charge only from the FeS{111} and Fe_3O_4{001} and {111} surfaces, where the CO_2 molecule is chemisorbed, as shown in table 4. We found that $\triangle q$ is between −0.17 and −0.80 e^- for the chemisorbed modes of the CO_2 molecule. The largest charge transfer to the chemisorbed CO_2 molecule occurred at the FeS{111} surface, as the interacting Fe^{2+} ions are oxidized to Fe^{3+} ions in the presence of adsorbing species including oxygen and water [72,82]. Similar amounts of charge transfer have been reported to occur between chemisorbed CO_2 and the FeS(011) surface [51]. However, the {111} surfaces of FeS and Fe_3O_4 are always more prone to larger donations of electronic charge than the {001} planes of these minerals, in agreement with the lower value of the work function
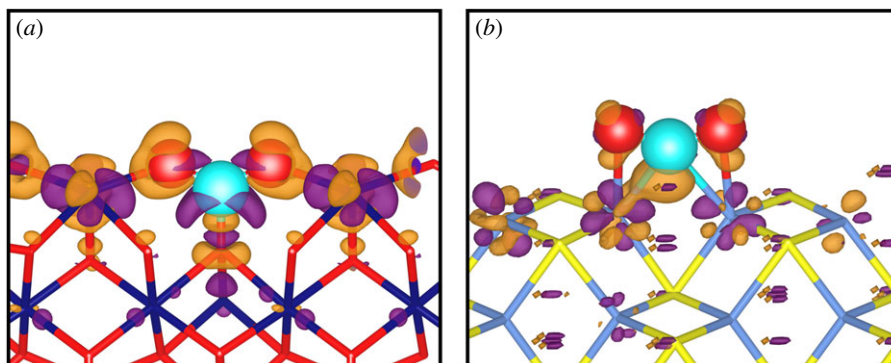
Figure 5. Charge density flow (ρ) for the CO_2 molecule adsorbed on (a) the $Fe_3O_4\{111\}$ and (b) the $FeS\{111\}$ surfaces. Electron density gain and depletion surfaces are in orange and purple, respectively. Isosurfaces display a value of $\pm 0.009\,e\,\text{Å}^{-3}$. Tetrahedral Fe_A atoms are in light blue, octahedral Fe_B atoms are in dark blue, S atoms are in yellow, C atoms are in cyan and O atoms are in red. Surface atoms are represented as sticks and the CO_2 molecule is represented as balls and sticks. (Online version in colour.)

(Φ) of the $\{111\}$ surfaces, which measures the energy required to bring a surface electron to the vacuum. The larger bending of the CO_2 apex angle correlates with the larger charge transfer to this molecule from the $\{111\}$ than from the $\{001\}$ surface for both FeS and Fe_3O_4, but this trend fails when they are compared globally. This can be visualized in a charge density flow scheme, representing the electron density changes on the adsorption of a CO_2 molecule. Figure 5 illustrates the rearrangement of the electronic cloud upon adsorption of the CO_2 molecule on the $Fe_3O_4\{111\}$ and $FeS\{111\}$ surfaces. For the two cases, the negative charge accumulates on the O atoms of the adsorbate, activating this molecule and triggering structural changes, such as the reduction of the CO_2 apex angle and elongation of the $C-O$ bond distances (table 2). Our simulations also suggest a negligible electron transfer for the physisorbed interactions of the CO_2 molecule with the $FeS\{001\}$ and $Fe_3S_4\{001\}$ and $\{111\}$ surfaces, which are, therefore, not discussed here.

(d) Simulated vibrational modes

Table 4 shows the wavenumbers of the fundamental vibrational modes of the isolated and adsorbed CO_2 molecule on the $\{001\}$ and $\{111\}$ surfaces of the three materials. There is an excellent agreement between the experimental and calculated stretching modes (ν) for the CO_2 molecule, with the largest difference being $24\,\text{cm}^{-1}$ for ν_{asym}, which is sufficiently accurate for the prediction of vibrational frequencies [77]. The asymmetric and symmetric CO stretching modes of the chemisorbed CO_2 indicate a notable red-shift with respect to the isolated molecule, in agreement with the weakening and stretching of the intramolecular CO bond. Interestingly, the difference vanishes for the wavenumbers of the isolated and physisorbed CO_2 molecule, which is in line with the lack of negative electronic transfer from the surface to the adsorbate.

At this point, it is possible to generalize that altogether (i) the smaller frequencies of the stretching modes for the chemisorbed CO_2, with respect to the isolated molecule, along with (ii) the elongation of the intramolecular $C-O$ bond and (iii) the localization of negative electronic charge at the molecular O atom lend support to the activation of the adsorbate, which could lead to further chemical transformations. In the following section, we focus on discussing the simplest unimolecular chemical reaction, in which the activated CO_2 molecule dissociates into CO and O fragments.

(e) Catalytic CO_2 dissociation

From our DFT simulations, we have inferred that the CO_2 molecule releases the largest adsorption energies when it interacts with both planes of Fe_3O_4 and the $FeS\{111\}$ surface. We are now
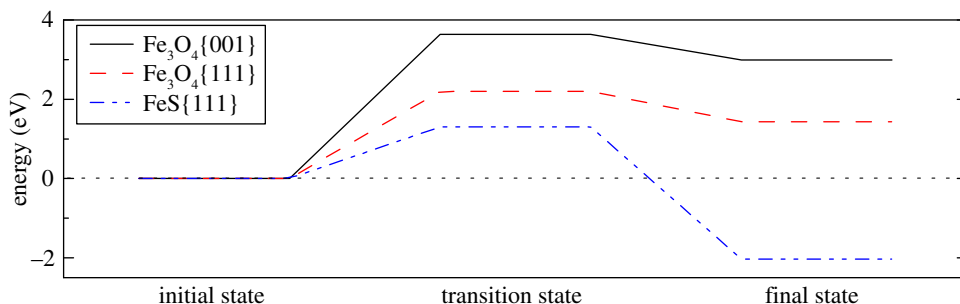
Figure 6. Reaction profile for the dissociation of the CO_2 molecule on the Fe_3O_4{001} and {111} and FeS{001} surfaces. (Online version in colour.)

interested in quantifying the reactivity towards dissociation of the activated and chemisorbed CO_2 molecule by analysing energetic and geometrical structural changes. The molecularly adsorbed configurations of the CO_2 on the Fe_3O_4 and FeS surfaces where the apex angle is bent are defined as the initial state or reactant. Figure 6 shows the reaction energy for the CO_2 dissociation on the different mineral surfaces and the activation energy required for this process to take place. It can be seen that on the FeS{111} surface, where the CO_2 molecule is chemisorbed, the dissociation energy (E_{diss}) is negative, while this process is strongly endothermic for Fe_3O_4{001} and {111} surfaces. The highly exothermic dissociation of CO_2 at the FeS{111} surface along with the relatively low activation barrier of 1.30 eV can be attributed to the stronger binding of the CO and O fragments to bridging Fe sites or to the instability of the CO_2 molecule on this surface. This suggests that, under low CO_2 pressures, the FeS{111} favours dissociative adsorption over molecular adsorption, although this process is not as effective as on α-Mo_2C, one of the most widely studied transition metal carbides for CO_2 conversion [114], where the activation energies can be 1.04 eV lower [115]. On the other hand, dissociation of the CO_2 molecule on any of the Fe_3O_4 surfaces is unlikely to take place, because not only are the activation energies relatively large but also the dissociation energies are very endothermic.

4. Conclusions

We have carried out a series of DFT simulations to study CO_2 adsorption and dissociation on the {001} and {111} surfaces of three iron-bearing minerals with different stoichiometry and structure. Our results indicate that the strongest adsorption takes place when the CO_2 molecule coordinates several surface atoms.

In general, we have found that the energetically most favourable interfacial system occurs when the CO_2 molecule interacts with the Fe_3O_4{111} surface. Our calculations suggest that, in the relaxed structures of the CO_2/mineral systems, the initially linear adsorbate molecule bends its geometry, forming an $\angle$OCO of around 130°, only when it receives electronic charge from the mineral surface. Although the FeS{111} surface is the largest donor of electronic charge due to its low work function and low electronegativity of the S atoms, there is a trend between the charge gained by the CO_2 molecule and the adsorption energy for the Fe_3O_4 surfaces. Changes in the simulated vibrational frequencies of the C−O bond from the isolated to the chemisorbed CO_2 molecule indicate the weakening of this bond. CO_2 dissociation can only happen spontaneously on the FeS{111} surface due to the availability of electrons to activate the molecule. Although the Fe_3O_4{001} and {111} surfaces also transfer electronic charge to the CO_2 molecule upon adsorption, this is not large enough to induce the activation required for dissociation.

Our simulations show that the adsorption of CO_2 to Fe_3S_4{111} and the main surfaces of FeS and Fe_3O_4 is exothermic, indicating that this molecule can be effectively captured by these materials.

12

rsta.royalsocietypublishing.org Phil. Trans. R. Soc. A 376: 20170065

Future work will focus on simulating the effect of temperature and CO_2 partial pressure via molecular dynamics simulations, as well as calculating the adsorption of H_2O on these minerals, to consider the effect of this ubiquitous molecule on the formation of a passivating carbonate layer on the surfaces of Fe_3O_4, Fe_3S_4 and FeS.

References

1. United Nations. Framework Convention on Climate Change. 2015 *Adoption of the Paris Agreement*. Report FCCC/CP/2015/L.9Rev.1. Paris, France: UNFCCC. Available from: http://unfccc.int/resource/docs/2015/cop21/eng/l09r01.pdf.

2. United Nations. 1998 *Kyoto Protocol to the United Nations Framework Convention on Climate Change*. Kyoto, Japan: UNFCCC. Available from: http://unfccc.int/resource/docs/convkp/kpeng.pdf.

3. Lüthi D *et al.* 2008 High-resolution carbon dioxide concentration record 650 000–800 000 years before present. *Nature* **453**, 379–382. (doi:10.1038/nature06949)

4. Shakun JD, Clark PU, He F, Marcott SA, Mix AC, Liu Z, Otto-Bliesner B, Schmittner A, Bard E. 2012 Global warming preceded by increasing carbon dioxide concentrations during the last deglaciation. *Nature* **484**, 49–54. (doi:10.1038/nature10915)

5. Aresta M, Dibenedetto A, Quaranta E. 2016 State of the art and perspectives in catalytic processes for CO_2 conversion into chemicals and fuels: the distinctive contribution of chemical catalysis and biotechnology. *J. Catal.* **343**, 2–45. (doi:10.1016/j.jcat.2016.04.003)

6. Meylan FD, Moreau V, Erkman S. 2015 CO_2 utilization in the perspective of industrial ecology, an overview. *J. CO$_2$ Utiliz.* **12**, 101–108. (doi:10.1016/j.jcou.2015.05.003)

7. Aresta M, Dibenedetto A, Angelini A. 2014 Catalysis for the valorization of exhaust carbon: from CO_2 to chemicals, materials, and fuels. Technological use of CO_2. *Chem. Rev.* **114**, 1709–1742. (doi:10.1021/cr4002758)

8. Aresta M, Dibenedetto A, Angelini A. 2013 The changing paradigm in CO_2 utilization. *J. CO$_2$ Utiliz.* **3–4**, 65–73. (doi:10.1016/j.jcou.2013.08.001)

9. Aresta M. 2010 Carbon dioxide: utilization options to reduce its accumulation in the atmosphere. In *Carbon dioxide as chemical feedstock* (ed. M Aresta), ch. 1, pp. 1–13. Weinheim, Germany: Wiley-VCH. (doi:10.1002/9783527629916.ch1)

10. Quaranta E, Aresta M. 2010 The chemistry of N–CO_2 bonds: synthesis of carbamic acids and their derivatives, isocyanates, and ureas. In *Carbon dioxide as chemical feedstock* (ed. M Aresta), ch. 6, pp. 121–167. Weinheim, Germany: Wiley-VCH. (doi:10.1002/9783527629916.ch6)

11. Dell'Amico DB, Calderazzo F, Labella L, Marchetti F, Pampaloni G. 2003 Converting carbon dioxide into carbamato derivatives. *Chem. Rev.* **103**, 3857–3898. (doi:10.1021/cr940266m)

12. Bart SC, Anthon C, Heinemann FW, Bill E, Edelstein NM, Meyer K. 2008 Carbon dioxide activation with sterically pressured mid- and high-valent uranium complexes. *J. Am. Chem. Soc.* **130**, 12 536–12 546. (doi:10.1021/ja804263w)

13. Bramsen F, Bond AD, McKenzie CJ, Hazell RG, Moubaraki B, Murray KS. 2005 Self-assembly of the octanuclear cluster $[Cu_8(OH)_{10}(NH_2(CH_2)_2CH_3)_{12}]^{6+}$ and the one-dimensional N-propylcarbamate-linked coordination polymer $\{[Cu(O_2CNH(CH_2)_2CH_3)(NH_2(CH_2)_2CH_3)_3](ClO_4)\}_n$. *Chem. Eur. J.* **11**, 825–831. (doi:10.1002/chem.200400555)

13

rsta.royalsocietypublishing.org   Phil. Trans. R. Soc. A **376**: 20170065

14. Ballivet-Tkatchenko D, Dibenedetto A. 2010 Synthesis of linear and cyclic carbonates. In *Carbon dioxide as chemical feedstock* (ed. M Aresta), ch. 7, pp. 169–212. Weinheim, Germany: Wiley-VCH. (doi:10.1002/9783527629916.ch7)

15. Darensbourg DJ, Andreatta JR, Moncada AI. 2010 Polymers from carbon dioxide: polycarbonates, polythiocarbonates, and polyurethanes. In *Carbon dioxide as chemical feedstock* (ed. M Aresta), ch. 8, pp. 213–248. Weinheim, Germany: Wiley-VCH. (doi:10.1002/9783527629916.ch8)

16. Sugimoto H, Inoue S. 2005 Recent progress in the synthesis of polymers based on carbon dioxide. *J. Fudan Univ.* (*Nat. Sci.*) **44**, 640–641. (doi:10.1351/pac200678101823)

17. Lee BY, Kwon HY, Lee SY, Na SJ, Han Si, Yun H, Lee H, Park Y-W. 2005 Bimetallic anilido-aldimine zinc complexes for epoxide/CO_2 copolymerization. *J. Am. Chem. Soc.* **127**, 3031–3037. (doi:10.1021/ja0435135)

18. Xiao Y, Wang Z, Ding K. 2005 Copolymerization of cyclohexene oxide with CO_2 by using intramolecular dinuclear zinc catalysts. *Chem. Eur. J.* **11**, 3668–3678. (doi:10.1002/chem.200401159)

19. Darensbourg DJ, Yarbrough JC. 2002 Mechanistic aspects of the copolymerization reaction of carbon dioxide and epoxides, using a chiral salen chromium chloride catalyst. *J. Am. Chem. Soc.* **124**, 6335–6342. (doi:10.1021/ja012714v)

20. Stamp LM, Mang SA, Holmes AB, Knights KA, de Miguel YR, McConvey IF. 2001 Polymer supported chromium porphyrin as catalyst for polycarbonate formation in supercritical carbon dioxide. *Chem. Commun.* **2001**, 2502–2503. (doi:10.1039/B107400H)

21. Qin Z, Thomas CM, Lee S, Coates GW. 2003 Cobalt-based complexes for the copolymerization of propylene oxide and CO_2: active and selective catalysts for polycarbonate synthesis. *Angew. Chem. Int. Edn* **42**, 5484–5487. (doi:10.1002/anie.200352605)

22. Lu XB, Wang Y. 2004 Highly active, binary catalyst systems for the alternating copolymerization of CO_2 and epoxides under mild conditions. *Angew. Chem. Int. Edn* **43**, 3574–3577. (doi:10.1002/anie.200453998)

23. Centi G, Perathoner S. 2009 Catalysis: role and challenges for a sustainable energy. *Top. Catal.* **52**, 948–961. (doi:10.1007/s11244-009-9245-x)

24. Bensaid S, Centi G, Garrone E, Perathoner S, Saracco G. 2012 Towards artificial leaves for solar hydrogen and fuels from carbon dioxide. *ChemSusChem* **5**, 500–521. (doi:10.1002/cssc.201100661)

25. Ampelli C, Centi G, Passalacqua R, Perathoner S. 2010 Synthesis of solar fuels by a novel photoelectrocatalytic approach. *Energy Environ. Sci.* **3**, 292–301. (doi:10.1039/B925470F)

26. Hirunsit P, Soodsawang W, Limtrakul J. 2015 CO_2 electrochemical reduction to methane and methanol on copper-based alloys: theoretical insight. *J. Phys. Chem. C* **119**, 8238–8249. (doi:10.1021/acs.jpcc.5b01574)

27. Centi G, Perathoner S. 2009 Opportunities and prospects in the chemical recycling of carbon dioxide to fuels. *Catal. Today* **148**, 191–205. (doi:10.1016/j.cattod.2009.07.075)

28. Centi G, Perathoner S. 2010 Towards solar fuels from water and CO_2. *ChemSusChem* **3**, 195–208. (doi:10.1002/cssc.200900289)

29. Aresta M, Quaranta E, Tommasi I, Giannoccaro P, Ciccarese A. 1995 Enzymatic versus chemical carbon dioxide utilization. 1. The role of metal centres in carboxylation reactions. *Gazz. Chim. Ital.* **125**, 509–538.

30. Cornell RM, Schwertmann U. 2003 *The iron oxides*, 2nd edn. Weinheim, Germany: Wiley-VCH. (doi:10.1002/3527602097)

31. Topham S. 1985 The history of the catalytic synthesis of ammonia. In *Catalysis: science and technology* (ed. JR Anderson), vol. 7, pp. 1–50. Berlin, Germany: Springer.

32. Almquist JA, Crittenden ED. 1926 A study of pure-iron and promoted-iron catalysts for ammonia synthesis. *Ind. Eng. Chem.* **18**, 1307–1309. (doi:10.1021/ie50204a036)

33. Aika Ki, Yamaguchi J, Ozaki A. 1973 Ammonia synthesis over rhodium, iridium and platinum promoted by potassium. *Chem. Lett.* **2**, 161–164. (doi:10.1246/cl.1973.161)

34. Logan SR, Kemball C. 1960 The catalytic decomposition of ammonia on evaporated metal films. *Trans. Faraday Soc.* **56**, 144–153. (doi:10.1039/tf9605600144)

35. Appl M. 2012 Ammonia, 1. Introduction. In *Ullmann's encyclopedia of industrial chemistry* (ed. B Elvers), pp. 107–137. Weinheim, Germany: Wiley-VCH. (doi:10.1002/14356007.a02_143.pub3)

36. Spencer ND, Schoonmaker RC, Somorjai GA. 1982 Iron single crystals as ammonia synthesis catalysts: effect of surface structure on catalyst activity. *J. Catal.* **74**, 129–135. (doi:10.1016/0021-9517(82)90016-1)

37. Emmett PH, Brunauer S. 1934 The adsorption of nitrogen by iron synthetic ammonia catalysts. *J. Am. Chem. Soc.* **56**, 35–41. (doi:10.1021/ja01316a011)

38. Scholten JJF, Zwietering P, Konvalinka JA, de Boer JH. 1959 Chemisorption of nitrogen on iron catalysts in connection with ammonia synthesis. Part 1.–The kinetics of the adsorption and desorption of nitrogen. *Trans. Faraday Soc.* **55**, 2166–2179. (doi:10.1039/TF9595502166)

39. Aparicio LM, Dumesic JA. 1994 Ammonia synthesis kinetics: surface chemistry, rate expressions, and kinetic analysis. *Top. Catal.* **1**, 233–252. (doi:10.1007/BF01492278)

40. Kaneko T, Derbyshire F, Makino E, Gray D, Tamura M, Li K. 2012 Coal liquefaction. In *Ullmann's encyclopedia of industrial chemistry* (ed. B Elvers), pp. 1–83. Weinheim, Germany: Wiley-VCH. (doi:10.1002/14356007.a07_197.pub2)

41. Satterfield CN, Hanlon RT, Tung SE, Zou ZM, Papaefthymiou GC. 1986 Effect of water on the iron-catalyzed Fischer–Tropsch synthesis. *Ind. Eng. Chem. Prod. Res. Dev.* **25**, 407–414. (doi:10.1021/i300023a007)

42. Gonzalez JC, Gonzalez MG, Laborde MA, Moreno N. 1986 Effect of temperature and reduction on the activity of high temperature water gas shift catalysts. *Appl. Catal.* **20**, 3–13. (doi:10.1016/0166-9834(86)80005-7)

43. Russell MJ, Martin W. 2004 The rocky roots of the acetyl-CoA pathway. *Trends. Biochem. Sci.* **29**, 358–363. (doi:10.1016/j.tibs.2004.05.007)

44. Cody GD. 2004 Transition metal sulfides and the origins of metabolism. *Annu. Rev. Earth Planet. Sci.* **32**, 569–599. (doi:10.1146/annurev.earth.32.101802.120225)

45. Martin W, Baross J, Kelley D, Russell MJ. 2008 Hydrothermal vents and the origin of life. *Nat. Rev. Microbiol.* **6**, 805–814. (doi:10.1038/nrmicro1991)

46. Huber C, Wächtershäuser G. 1997 Activated acetic acid by carbon fixation on (Fe,Ni)S under primordial conditions. *Science* **276**, 245–247. (doi:10.1126/science.276.5310.245)

47. Russell MJ, Hall AJ. 1997 The emergence of life from iron monosulphide bubbles at a submarine hydrothermal redox and pH front. *J. Geol. Soc. London.* **154**, 377–402. (doi:10.1144/gsjgs.154.3.0377)

48. Wächtershäuser G. 1992 Groundworks for an evolutionary biochemistry: the iron–sulphur world. *Prog. Biophys. Mol. Biol.* **58**, 85–201. (doi:10.1016/0079-6107(92)90022-X)

49. Ferry JG. 1995 CO dehydrogenase. *Annu. Rev. Microbiol.* **49**, 305–333. (doi:10.1146/annurev.mi.49.100195.001513)

50. Roldan A *et al.* 2015 Bio-inspired CO_2 conversion by iron sulfide catalysts under sustainable conditions. *Chem. Commun.* **51**, 7501–7504. (doi:10.1039/C5CC02078F)

51. Dzade NY, Roldan A, de Leeuw NH. 2015 Activation and dissociation of CO_2 on the (001), (011), and (111) surfaces of mackinawite (FeS): a dispersion-corrected DFT study. *J. Chem. Phys.* **143**, 094703. (doi:10.1063/1.4929470)

52. Roldan A, de Leeuw NH. 2016 Methanol formation from CO_2 catalyzed by $Fe_3S_4\{111\}$: formate versus hydrocarboxyl pathways. *Faraday Discuss.* **188**, 161–180. (doi:10.1039/C5FD00186B)

53. Kresse G, Hafner J. 1993 *Ab initio* molecular dynamics for liquid metals. *Phys. Rev. B* **47**, 558–561. (doi:10.1103/PhysRevB.47.558)

54. Kresse G, Hafner J. 1994 *Ab initio* molecular-dynamics simulation of the liquid-metal–amorphous-semiconductor transition in germanium. *Phys. Rev. B* **49**, 14 251–14 269. (doi:10.1103/PhysRevB.49.14251)

55. Kresse G, Furthmüller J. 1996 Efficient iterative schemes for *ab initio* total-energy calculations using a plane-wave basis set. *Phys. Rev. B* **54**, 11169–11186. (doi:10.1103/PhysRevB.54.11169)

56. Kresse G, Furthmüller J. 1996 Efficiency of *ab-initio* total energy calculations for metals and semiconductors using a plane-wave basis set. *Comput. Mater. Sci.* **6**, 15–50. (doi:10.1016/0927-0256(96)00008-0)

57. Perdew JP, Burke K, Ernzerhof M. 1996 Generalized gradient approximation made simple. *Phys. Rev. Lett.* **77**, 3865–3868. (doi:10.1103/PhysRevLett.77.3865)

58. Perdew JP, Burke K, Ernzerhof M. 1997 Errata: Generalized gradient approximation made simple. [*Phys. Rev. Lett.* **77**, 3865 (1996)]. *Phys. Rev. Lett.* **78**, 1396. (doi:10.1103/PhysRevLett.78.1396)

59. Perdew JP, Chevary JA, Vosko SH, Jackson KA, Pederson MR, Singh DJ, Fiolhais C. 1992 Atoms, molecules, solids, and surfaces: applications of the generalized gradient approximation for exchange and correlation. *Phys. Rev. B* **46**, 6671–6687. (doi:10.1103/PhysRevB.46.6671)

60. Perdew JP, Chevary JA, Vosko SH, Jackson KA, Pederson MR, Singh DJ, Fiolhais C. 1993 Erratum: Atoms, molecules, solids, and surfaces: applications of the generalized gradient approximation for exchange and correlation [*Phys. Rev. B* **46**, 6671 (1992)]. *Phys. Rev. B* **48**, 4978. (doi:10.1103/PhysRevB.48.4978.2)

61. Vosko SH, Wilk L, Nusair M. 1980 Accurate spin-dependent electron liquid correlation energies for local spin density calculations: a critical analysis. *Can. J. Phys.* **58**, 1200–1211. (doi:10.1139/p80-159)

62. Grimme S. 2006 Semiempirical GGA-type density functional constructed with a long-range dispersion correction. *J. Comput. Chem.* **27**, 1787–1799. (doi:10.1002/jcc.20495)

63. Santos-Carballal D, Roldan A, Grau-Crespo R, de Leeuw NH. 2014 A DFT study of the structures, stabilities and redox behaviour of the major surfaces of magnetite Fe_3O_4. *Phys. Chem. Chem. Phys.* **16**, 21 082–21 097. (doi:10.1039/c4cp00529e)

64. Tafreshi SS, Roldan A, Dzade NY, de Leeuw NH. 2014 Adsorption of hydrazine on the perfect and defective copper (111) surface: a dispersion-corrected DFT study. *Surf. Sci.* **622**, 1–8. (doi:10.1016/j.susc.2013.11.013)

65. Terranova U, de Leeuw NH. 2014 Aqueous Fe_2S_2 cluster: structure, magnetic coupling, and hydration behaviour from Hubbard U density functional theory. *Phys. Chem. Chem. Phys.* **16**, 13 426–13 433. (doi:10.1039/c4cp00984c)

66. Dzade NY, Roldan A, de Leeuw NH. 2014 The surface chemistry of NO_x on mackinawite (FeS) surfaces: a DFT-D2 study. *Phys. Chem. Chem. Phys.* **16**, 15 444–15 456. (doi:10.1039/c4cp01138d)

67. Santos-Carballal D, Roldan A, Grau-Crespo R, de Leeuw NH. 2015 First-principles study of the inversion thermodynamics and electronic structure of FeM_2X_4 (thio)spinels ($M = Cr$, Mn, Co, Ni; $X = O$, S). *Phys. Rev. B* **91**, 195106. (doi:10.1103/PhysRevB.91.195106)

68. Haider S, Roldan A, de Leeuw NH. 2014 Catalytic dissociation of water on the (001), (011), and (111) surfaces of violarite, $FeNi_2S_4$: a DFT-D2 study. *J. Phys. Chem. C* **118**, 1958–1967. (doi:10.1021/jp409522q)

69. Dzade NY, Roldan A, de Leeuw NH. 2013 Adsorption of methylamine on mackinawite (FeS) surfaces: a density functional theory study. *J. Chem. Phys.* **139**, 124708. (doi:10.1063/1.4822040)

70. Kresse G, Joubert D. 1999 From ultrasoft pseudopotentials to the projector augmented-wave method. *Phys. Rev. B* **59**, 1758–1775. (doi:10.1103/PhysRevB.59.1758)

71. Blöchl PE. 1994 Projector augmented-wave method. *Phys. Rev. B* **50**, 17 953–17 979. (doi:10.1103/PhysRevB.50.17953)

72. Dzade NY, Roldan A, de Leeuw NH. 2016 DFT-D2 study of the adsorption and dissociation of water on clean and oxygen-covered {001} and {011} surfaces of mackinawite (FeS). *J. Phys. Chem. C* **120**, 21 441–21 450. (doi:10.1021/acs.jpcc.6b06122)

73. Dzade NY, Roldan A, de Leeuw NH. 2017 Structures and properties of $As(OH)_3$ adsorption complexes on hydrated mackinawite (FeS) surfaces: a DFT-D2 study. *Environ. Sci. Technol.* **51**, 3461–3470. (doi:10.1021/acs.est.7b00107)

74. Devey AJ, Grau-Crespo R, de Leeuw NH. 2008 Combined density functional theory and interatomic potential study of the bulk and surface structures and properties of the iron sulfide mackinawite (FeS). *J. Phys. Chem. C* **112**, 10 960–10 967. (doi:10.1021/jp8001959)

75. Devey AJ, Grau-Crespo R, de Leeuw NH. 2009 Electronic and magnetic structure of Fe_3S_4: GGA+U investigation. *Phys. Rev. B* **79**, 195126. (doi:10.1103/PhysRevB.79.195126)

76. Roldan A, Santos-Carballal D, de Leeuw NH. 2013 A comparative DFT study of the mechanical and electronic properties of greigite Fe_3S_4 and magnetite Fe_3O_4. *J. Chem. Phys.* **138**, 204712. (doi:10.1063/1.4807614)

77. Santos-Carballal D, Roldan A, de Leeuw NH. 2016 Early oxidation processes on the greigite Fe_3S_4(001) surface by water: a density functional theory study. *J. Phys. Chem. C* **120**, 8616–8629. (doi:10.1021/acs.jpcc.6b00216)

78. Roldan A, de Leeuw NH. 2016 Catalytic water dissociation by greigite Fe_3S_4 surfaces: density functional theory study. *Proc. R. Soc. A* **472**, 20160080. (doi:10.1098/rspa.2016.0080)

79. Roldan A, de Leeuw NH. 2017 A kinetic model of water adsorption, clustering and dissociation on the Fe_3S_4{001} surface. *Phys. Chem. Chem. Phys.* **19**, 12 045–12 055. (doi:10.1039/C6CP07371A)

80. Anisimov VI, Korotin MA, Zaanen J, Andersen OK. 1992 Spin bags, polarons, and impurity potentials in $La_{2-x}Sr_xCuO_4$ from first principles. *Phys. Rev. Lett.* **68**, 345–348. (doi:10.1103/PhysRevLett.68.345)

81. Dudarev SL, Botton GA, Savrasov SY, Humphreys CJ, Sutton AP. 1998 Electron-energy-loss spectra and the structural stability of nickel oxide: an LSDA+U study. *Phys. Rev. B* **57**, 1505–1509. (doi:10.1103/PhysRevB.57.1505)

82. Dzade NY, Roldan A, de Leeuw NH. 2016 DFT-D2 simulations of water adsorption and dissociation on the low-index surfaces of mackinawite (FeS). *J. Chem. Phys.* **144**, 174704. (doi:10.1063/1.4947588)

83. Haider S, Grau-Crespo R, Devey AJ, de Leeuw NH. 2012 Cation distribution and mixing thermodynamics in Fe/Ni thiospinels. *Geochim. Cosmochim. Acta* **88**, 275–282. (doi:10.1016/j.gca.2012.04.007)

84. Makov G, Payne MC. 1995 Periodic boundary conditions in *ab initio* calculations. *Phys. Rev. B* **51**, 4014–4022. (doi:10.1103/PhysRevB.51.4014)

85. Neugebauer J, Scheffler M. 1992 Adsorbate–substrate and adsorbate–adsorbate interactions of Na and K adlayers on Al(111). *Phys. Rev. B* **46**, 16 067–16 080. (doi:10.1103/PhysRevB.46.16067)

86. Blöchl PE, Jepsen O, Andersen OK. 1994 Improved tetrahedron method for Brillouin-zone integrations. *Phys. Rev. B* **49**, 16223. (doi:10.1103/PhysRevB.49.16223)

87. Henkelman G, Arnaldsson A, Jónsson H. 2006 A fast and robust algorithm for Bader decomposition of charge density. *Comput. Mater. Sci.* **36**, 354–360. (doi:10.1016/j.commatsci.2005.04.010)

88. Sanville E, Kenny SD, Smith R, Henkelman G. 2007 Improved grid-based algorithm for Bader charge allocation. *J. Comput. Chem.* **28**, 899–908. (doi:10.1002/jcc.20575)

89. Tang W, Sanville E, Henkelman G. 2009 A grid-based Bader analysis algorithm without lattice bias. *J. Phys.: Condens. Matter* **21**, 084204. (doi:10.1088/0953-8984/21/8/084204)

90. Henkelman G, Uberuaga BP, Jónsson H. 2000 A climbing image nudged elastic band method for finding saddle points and minimum energy paths. *J. Chem. Phys.* **113**, 9901–9904. (doi:10.1063/1.1329672)

91. Henkelman G, Jónsson H. 2000 Improved tangent estimate in the nudged elastic band method for finding minimum energy paths and saddle points. *J. Chem. Phys.* **113**, 9978–9985. (doi:10.1063/1.1323224)

92. Jónsson H, Mills G, Jacobsen KW. 1998 Nudged elastic band method for finding minimum energy paths of transitions. In *Classical and quantum dynamics in condensed phase simulations* (eds BJ Berne, G Ciccotti, DF Coker). Proc. Int. School of Physics, ch. 16, pp. 385–404. Singapore: World Scientific. (doi:10.1142/9789812839664_0016)

93. Sheppard D, Terrell R, Henkelman G. 2008 Optimization methods for finding minimum energy paths. *J. Chem. Phys.* **128**, 134106. (doi:10.1063/1.2841941)

94. Henkelman G, Jóhannesson G, Jónsson H. 2002 Methods for finding saddle points and minimum energy paths. In *Theoretical methods in condensed phase chemistry* (ed. SD Schwartz), Progress in Theoretical Chemistry and Physics, ch. 10, vol. 5, pp. 269–300. Dordrecht, The Netherlands: Kluwer Academic. (doi:10.1007/0-306-46949-9_10)

95. Skinner BJ, Erd RC, Grimaldi FS. 1964 Greigite, the thio-spinel of iron; a new mineral. *Am. Mineral.* **49**, 543–555. Available from: http://www.minsocam.org/ammin/AM49/AM49_543.pdf.

96. Wright JP, Attfield JP, Radaelli PG. 2002 Charge ordered structure of magnetite Fe_3O_4 below the Verwey transition. *Phys. Rev. B* **66**, 214422. (doi:10.1103/PhysRevB.66.214422)

97. Surerus KK, Kennedy MC, Beinert H, Münck E. 1989 Mössbauer study of the inactive Fe_3S_4 and Fe_3Se_4 and the active Fe_4Se_4 forms of beef heart aconitase. *Proc. Natl Acad. Sci. USA* **86**, 9846–9850. (doi:10.1073/pnas.86.24.9846)

98. Vaughan DJ, Tossell JA. 1981 Electronic structure of thiospinel minerals: results from MO calculation. *Am. Mineral.* **66**, 1250–1253. Available from: http://www.minsocam.org/ammin/AM66/AM66_1250.pdf.

17

rsta.royalsocietypublishing.org Phil. Trans. R. Soc. A **376**: 20170065

99. Vaughan DJ, Craig JR. 1985 The crystal chemistry of iron–nickel thiospinels. *Am. Mineral.* **70**, 1036–1043. Available from: http://rruff.info/uploads/AM70_1036.pdf.

100. Chang L, Rainford BD, Stewart JR, Ritter C, Roberts AP, Tang Y, Chen Q. 2009 Magnetic structure of greigite (Fe_3S_4) probed by neutron powder diffraction and polarized neutron diffraction. *J. Geophys. Res.* **114**, B07101. (doi:10.1029/2008JB006260)

101. Dekkers MJ, Passier HF, Schoonen MAA. 2000 Magnetic properties of hydrothermally synthesized greigite (Fe_3S_4)–II. High- and low-temperature characteristics. *Geophys. J. Int.* **141**, 809–819. (doi:10.1046/j.1365-246x.2000.00129.x)

102. Néel L. 1948 Magnetic properties of ferrites: ferrimagnetism and antiferromagnetism. *Ann. Phys. Paris* **3**, 137–198.

103. Shull CG, Wollan EO, Koehler WC. 1951 Neutron scattering and polarization by ferromagnetic materials. *Phys. Rev.* **84**, 912–921. (doi:10.1103/PhysRev.84.912)

104. Lennie AR, Redfern SAT, Schofield PF, Vaughan DJ. 1995 Synthesis and Rietveld crystal structure Refinement of mackinawite, tetragonal FeS. *Mineral. Mag.* **59**, 677–683. (doi:10.1180/minmag.1995.059.397.10)

105. Berner RA. 1962 Tetragonal iron sulfide. *Science* **137**, 669–669. (doi:10.1126/science.137.3531.669-a)

106. Vaughan DJ, Craig JR. 1978 *Mineral chemistry of metal sulfides*. Cambridge, UK: Cambridge University Press.

107. Tasker PW. 1979 The stability of ionic crystal surfaces. *J. Phys. C: Solid State Phys.* **12**, 4977–4984. (doi:10.1088/0022-3719/12/22/036)

108. Watson GW, Kelsey ET, de Leeuw NH, Harris DJ, Parker SC. 1996 Atomistic simulation of dislocations, surfaces and interfaces in MgO. *J. Chem. Soc., Faraday Trans.* **92**, 433–438. (doi:10.1039/ft9969200433)

109. Lennie AR, Condon NG, Leibsle FM, Murray PW, Thornton G, Vaughan DJ. 1996 Structures of $Fe_3O_4(111)$ surfaces observed by scanning tunneling microscopy. *Phys. Rev. B* **53**, 10 244–10 253. (doi:10.1103/PhysRevB.53.10244)

110. Su T, Qin Z, Huang G, Ji H, Jiang Y, Chen J. 2016 Density functional theory study on the interaction of CO_2 with $Fe_3O_4(111)$ surface. *Appl. Surf. Sci.* **378**, 270–276. (doi:10.1016/j.apsusc.2016.03.097)

111. Pavelec J *et al.* 2017 A multi-technique study of CO_2 adsorption on Fe_3O_4 magnetite. *J. Chem. Phys.* **146**, 014701. (doi:10.1063/1.4973241)

112. Gamba O, Hulva J, Pavelec J, Bliem R, Schmid M, Diebold U, Parkinson GS. 2017 The role of surface defects in the adsorption of methanol on $Fe_3O_4(001)$. *Top. Catal.* **60**, 420–430. (doi:10.1007/s11244-016-0713-9)

113. Shimanouchi T. 1976 *Tables of molecular vibrational frequencies, Consolidated volume I*. Nat. Stand. Ref. Data Ser., Nat. Bur. Stand, 39. NSRDS-NBS-39, 164pp. See *NIST Chemistry WebBook*, NIST Standard Reference Database Number 69 (eds PJ Linstrom, WG Mallard). Gaithersburg, MD: National Institute of Standards and Technology. (doi:10.18434/T4D303)

114. Porosoff MD, Kattel S, Li W, Liu P, Chen JG. 2015 Identifying trends and descriptors for selective CO_2 conversion to CO over transition metal carbides. *Chem. Commun.* **51**, 6988–6991. (doi:10.1039/C5CC01545F)

115. Liu X, Kunkel C, Ramírez de la Piscina P, Homs N, Vines F, Illas F. 2017 Effective and highly selective CO generation from CO_2 using a polycrystalline α-Mo_2C catalyst. *ACS Catal.* **7**, 4323–4335. (doi:10.1021/acscatal.7b00735)